THE JOURNAL OF

Magnetism of Otherwise Nonmagnetic Elements: From Clusters to **Monolayers**

Manish Kumar Mohanta and Puru Jena*



Cite This: J. Phys. Chem. C 2024, 128, 12286-12295



Read Online

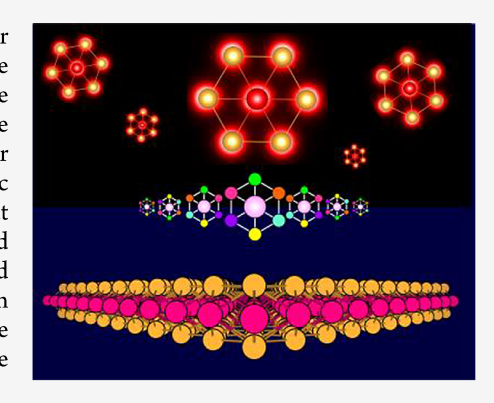
ACCESS I

Metrics & More

Article Recommendations

Supporting Information

ABSTRACT: Atomic clusters are known to exhibit properties different from their bulk phase. However, when assembled or supported on substrates, clusters often lose their uniqueness. For example, uranium and coinage metals (Cu, Ag, Au) are nonmagnetic in their bulk. Herein, we show that UX_6 (X= Cu, Ag, Au) clusters, unlike their nonmagnetic bulk, are not only magnetic but also retain their magnetic character and structure when assembled into a two-dimensional (2D) material. The magnetic moment remains localized at the U site and is found to be $3\mu_B$ in clusters and about $2\mu_{\rm B}$ in the 2D structure. In 2D UX₄ (X = Cu, Ag, Au) monolayers, U atoms are found to be coupled antiferromagnetically through an indirect exchange coupling mediated by the coinage metal atoms. Furthermore, hydrogenation of these monolayers can induce a transition from the antiferromagnetic to the ferromagnetic phase. These results, based on density functional theory, have predictive capability and can motivate experiments.



1. INTRODUCTION

Downloaded via VIRGINIA COMMONWEALTH UNIV on August 30, 2024 at 13:52:42 (UTC). See https://pubs.acs.org/sharingguidelines for options on how to legitimately share published articles

More than half of the elements in the periodic table possess nonzero spins, yet very few of them remain magnetic in their bulk phases. However, as their size is reduced, some of the clusters of nonmagnetic elements develop finite magnetic moments at the subnano meter length scale due to their large surface-to-volume ratio and reduced coordination number. One of the early observations where topology and symmetry were found to play a role in magnetism was in the Li4 cluster which has a spin-singlet ground state and a planar geometry but becomes a spin triplet configuration when it assumes a three-dimensional tetrahedral structure. This topology-driven magnetic transition was attributed to a delicate balance between Jahn-Teller distortion and Hund's rule coupling; the former favors a planar structure and zero spin while the latter favors a tetrahedral geometry and spin 1. Subsequently, transition metal atoms such as vanadium (V) and rhodium (Rh) that are nonmagnetic in the bulk were found to be magnetic in clusters.²⁻⁹ In addition, magnetic moments of transition metal elements get enhanced when their size is reduced to the nanoscale. While these results are firmly established by theory and experiment in isolated clusters, magnetism of otherwise nonmagnetic elements in the bulk form is rare.

In recent experimental work, Harris et al.11 studied the photoelectron spectroscopy of the UAu₆ cluster, intending to shed light on the UF₆ cluster which is an important material for the nuclear industry. However, previous experiments were not successful in understanding its electronic properties. As Au behaves like a halogen in small clusters, it was hoped that the study of UAu₆ could serve as a surrogate for UF₆. However, unlike the UF₆ cluster which has zero spin, the UAu₆ cluster was found to be magnetic with nearly $3\mu_{\rm B}$ magnetic moment localized at the U site. 11 In addition, UAu6 has three nearly degenerate isomers, all of which are magnetic irrespective of their geometry. This raises some fundamental questions. (1) Is it possible that similar clusters containing other coinage metal atoms such as Cu and Ag would become magnetic? Note that due to the relativistic effects, the properties of Au are different from those of Cu and Ag, including their color. (2) Can these clusters retain their geometry and magnetic properties, once assembled to form a crystal? (3) If so, would the coupling be ferromagnetic or antiferromagnetic? (4) Can magnetic coupling be altered by hydrogenation and/or biaxial strain? (5) What type of magnetic exchange interaction between localized spins dominates in these 2D structures?

In this work, we address the above questions. We show that UX_6 (X = Cu, Ag) clusters, analogous to the UAu₆ cluster, are magnetic with a magnetic moment of $3\mu_B$ localized at the Usite. The geometries as well as magnetism of the UX_6 (X = Cu, Ag, Au) clusters are retained, once they are assembled into a two-dimensional (2D) structure. The resulting UX_4 (X = Cu, Ag, Au) monolayers are antiferromagnetic but become ferromagnetic when hydrogenated. These results are based

Received: May 30, 2024 July 2, 2024 Revised: Accepted: July 3, 2024 Published: July 16, 2024





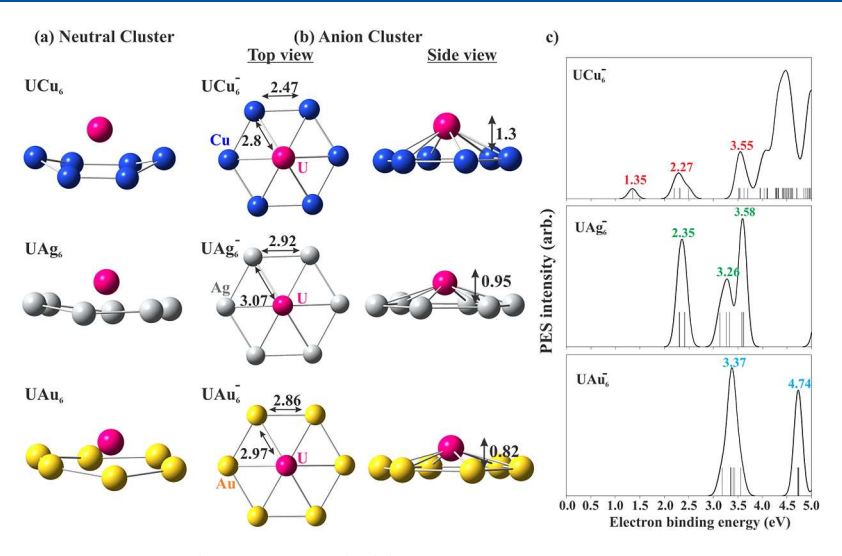


Figure 1. (a) Geometry of neutral UX_6 clusters (X = Cu, Ag, Au), (b) top and side view of the anionic UX_6 clusters; distance is in Å, the vertical distance between the U atom and the hexagonal plane is indicated in the figure, (c) calculated photoelectron spectra of UX_6 clusters.

on density functional theory which has been found to correctly account for the photoelectron spectroscopy (PES) experiments of isolated UAu_6 clusters. 11

2. COMPUTATIONAL DETAILS

The ground-state properties of isolated UX_6 (X = Cu, Ag, Au) clusters are calculated using spin unrestricted density functional theory (DFT) employed in the Gaussian16 package.¹ The exchange-correlation potential is treated using a Becke 3parameter Lee-Yang-Parr (B3LYP) hybrid functional. 13,14 The basis sets used for U and X (Cu, Ag, Au) atoms are correlation-consistent polarized valence double-ξ (cc-pVDZ-PP). 15,16 The scalar relativistic effects of the core electrons for U and X atoms are incorporated using 60-electron Stuttgart/ Cologne energy-consistent effective core potentials (ECP60MDF).^{17,18} Quadratic convergence algorithms are used during the optimization process without any symmetry constraints. The projected density of states, spin density, and photoelectron spectra of the clusters are calculated using the Multiwfn package. 19 The projected density of states (PDOS) is plotted using a Gaussian broadening function (full width at half-maximum, FWHM = 0.2 eV).

The ground state properties of 2D structures assembled from these clusters are calculated using the DFT incorporated in the Vienna ab initio Simulation Package (VASP). 20,21 The ion-electron interaction and the exchange-correlation potential are described by using the projector augmented wave (PAW)²² method and the generalized gradient approximation due to Perdew-Burke-Ernzerhof (GGA-PBE), 23 respectively. The effect of spin-orbit coupling (SOC) on the calculated magnetic properties is also taken into account. A kinetic energy cutoff of 500 eV is used. The first Brillouin zone is sampled by a Γ - centered 14 \times 14 \times 1 k-mesh for the unit cell and $10 \times 10 \times 1$ for the supercell. The GGA+U method²⁴ is adopted with an effective Hubbard $U_{\rm eff}$ value of 4 eV applied to the 5f orbitals of the uranium atom. We have also performed energy calculations with meta-GGA (SCAN) and $U_{\rm eff}$ value of 3 eV. The corresponding results are mentioned in the respective sections. A vacuum layer of 20 Å is added in the z-direction to avoid periodic interactions. The convergence criteria for the energy and force of each atom are set to 10⁻⁶ eV and 0.02 eV/Å, respectively. The PHONOPY code²⁵ is

used to obtain the phonon dispersion curve via the finite displacement method. The density of states (DOS) plots are analyzed using the VASPKIT²⁶ program. To study the interaction of hydrogen and Ag/Au surfaces at a higher temperature, ab initio molecular dynamics simulations (AIMD) are performed at 300 K for 2 ps using the Nosé–Hoover thermostat. The VMD,²⁷ Avogadro,²⁸ and VESTA²⁹ software are used to create the figures.

3. RESULTS AND DISCUSSION

In the following, we first discuss the geometry, electronic, and magnetic properties of isolated UX $_6$ (X = Cu, Ag, Au) clusters. Next, the stability and geometrical properties of 2D structures created by assembling these clusters are discussed. The magnetic properties of the 2D monolayers have been studied to correlate with the results obtained for isolated magnetic clusters. Further, the effect of hydrogenation on magnetic coupling is studied.

3.1. Ground-State Properties of UX_6 (X = Cu, Ag, Au) **Clusters.** In a recent joint experimental and theoretical work, Harris et al. 11 reported three stable nearly degenerate isomers of UAu₆ clusters among which the properties of the ring-like quasi-two-dimensional structure (six Au atoms forming a planar hexagonal ring with the U atom situated slightly above the center of the hexagon) was found to be consistent with experiment. We have used this geometry as a reference for the study of its iso-structural and iso-electronic UCu6 and UAg6 cousins. The optimized geometries of the neutral UX_6 (X = Cu, Ag, Au) clusters with top and side views are presented in Figure 1a. The dynamical stability of these clusters has been confirmed by the calculated positive vibrational frequencies. All six coinage metal atoms form a planar ring with the uranium atom located slightly above the center of the plane. The distances between X-X and X-U in the anionic clusters and the height of the U atom from the X₆ plane are indicated in Figure

The ground states of the UX_6^- anionic clusters have quartet spin multiplicity with a magnetic moment of $3\mu_B$ localized at the U site. The ground state of the UX_6 neutral clusters, on the other hand, is a spin quintet with a magnetic moment of $3\mu_B$ localized at the U site and $1\mu_B$ distributed over the X atoms. In Table S1 of the Supporting Information (SI), we have

provided the total energies of the spin singlet, triplet, and quintet state of UX_6 neutral and spin doublet and quartet state of the UX_6^- anion clusters. From the total energy values, the ground state of neutral and anionic clusters is found to be in quintet and quartet spin states, respectively. The electron affinities (EAs), defined as the energy difference between the ground vibronic states of the anion and the neutral, and the vertical detachment energy (VDE), defined as the energy difference between the anion and the neutral at the anion geometry, are given in Table 1. For reference, the values of calculated EA and VDE of the UAu_6 cluster in this work are in agreement with the reported experimental value. ¹¹

Table 1. Calculated Adiabatic Electron Affinity (EA) and Vertical Detachment Energy (VDE) of UX_6^- Clusters (X = Cu, Ag, Au)

| | EA (eV | 7) | VDE (eV | I) |
|-----------|-----------------|--------|-----------------|--------|
| clusters | experiment | theory | experiment | theory |
| UCu_6^- | | 1.29 | | 1.35 |
| UAg_6^- | | 2.21 | | 2.31 |
| UAu_6^- | 3.05 ± 0.05 | 3.07 | 3.28 ± 0.05 | 3.18 |

Next, the photoelectron spectra (PES) of UX_6^- clusters are theoretically simulated based on the generalized Koopman's theorem. The results are plotted in Figure 1c. The position of the first peak in the PES spectra is equivalent to the VDE of the system, as listed in Table 1. To check the accuracy, we note that the simulated first two peaks of UAu_6^- located at 3.37 and 4.74 eV are in excellent agreement with the experimental

photoelectron spectra. The location of the photoelectron intensity peaks for other anion clusters is indicated in Figure 1c.

Figure 2a,b depicts the natural population analysis (NPA) and spin population for UAu $_6$. The values of NPA charge and spin populations are listed in Table S2. Furthermore, Figure 2b and data in Table S2 indicate that spin-up electron populations are mainly localized on the uranium atom which is further confirmed by the spin-density contour plot in Figure 2c, whereas the Au-atom possesses a negligible spin population. The electron spin density distribution, calculated by using eq 1, is given as a contour plot on the XY-plane which confirms finite magnetization in the system originating from the localized spin at the U atom site. Here, α/β represents spin-up/spin-down which is also referred to as majority/minority electron spin.

$$\rho^{s}(r) = \rho^{\alpha}(r) - \rho^{\beta}(r) \tag{1}$$

From the electronic configuration of uranium and gold atoms (U: [Rn] $5f^3$ $6d^1$ $7s^2$; Au: [Xe] $6s^1$ $4f^{14}$ $5d^{10}$), it is quite evident that the HOMO and LUMO will be contributed by the s, d, and f orbitals of the uranium atom and the s/d-orbital of the Au-atom. The density of states (DOS), partial DOS (pDOS) and selected frontier orbitals of UAu_6^- are plotted in Figure 2d and those for the other two clusters are plotted in Figures S1 and S2. The HOMO–LUMO gaps of the majority spin-bands are found to be in decreasing trend UAu_6^- (2.19 eV) > UAg_6^- (1.71 eV) > UCu_6^- (0.34 eV). Furthermore, the pDOS plot indicates the percentage contribution of different atomic orbitals which are in accordance with the electronic

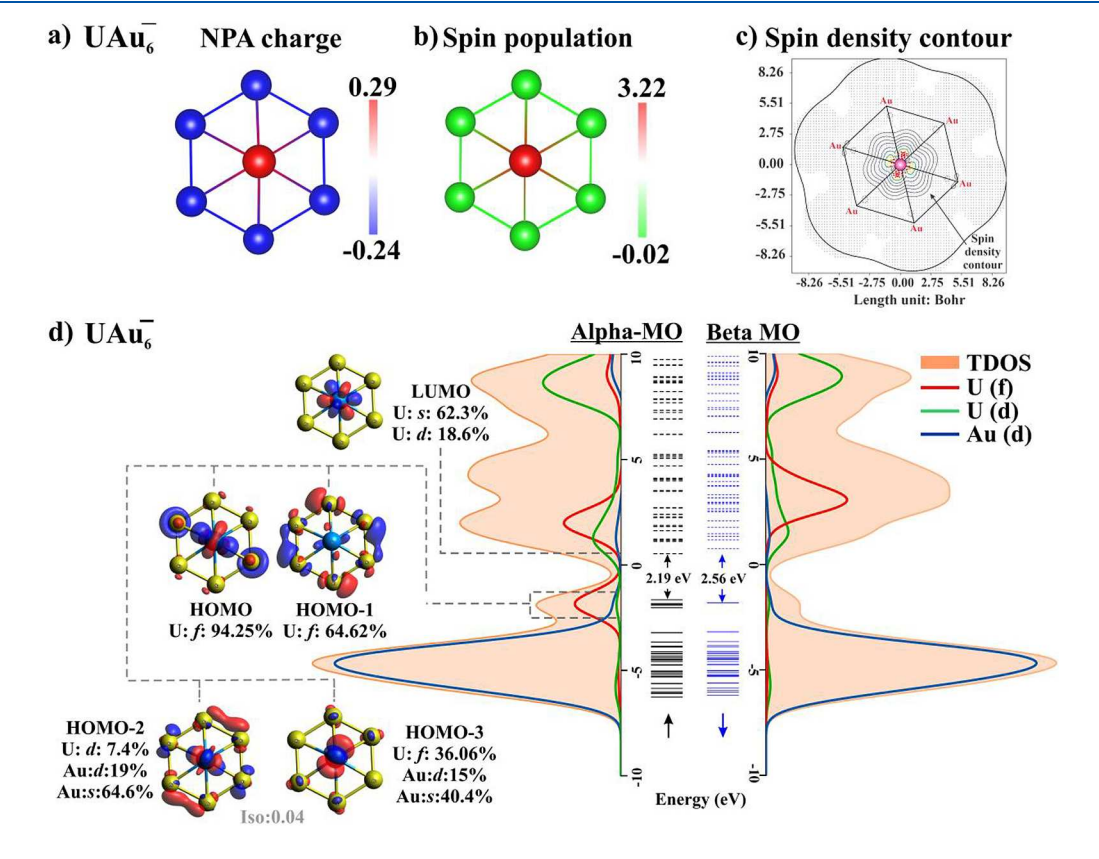


Figure 2. (a) Atomic charge distribution based on natural population analysis (NPA) of UAu_6^- , (b) spin population and magnetism analysis, (c) contour plot of the spin density on the XY-plane, (d) electronic structure analysis: partial density of states (pDOS) and selected α-orbitals of UAu_6^- ; solid/dashed lines indicate occupied/unoccupied molecular orbital.

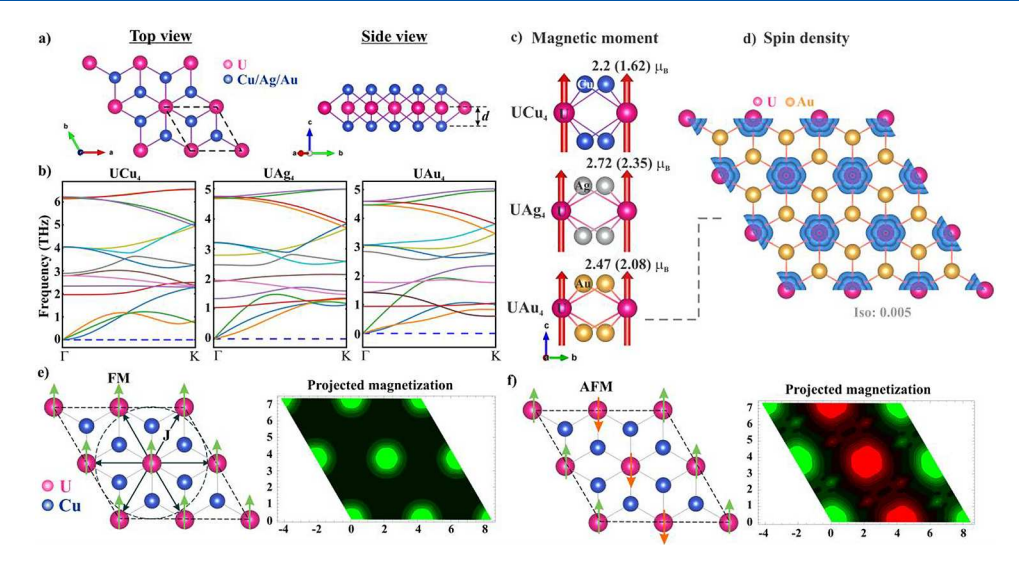


Figure 3. (a) Top and side view of the designed UX_4 unit cell and their (b) phonon dispersions (colors are random), (c) on-site magnetic moment at the U-site without (with) spin-orbit coupling, (d) spin-density plot of UAu_4 monolayer, (e,f) top view of FM/AFM state; green/red arrows indicate initialized magnetic moment ($\pm z$ -direction) at the U-site, and projected magnetization of spin density along the z-direction; green/red contours indicate localized spin-up/spin-down density, respectively.

configuration, as mentioned earlier. The orbital/atomic composition of the HOMO and LUMO for the majority and the minority spins are listed in Tables S3 and S4. Since the HOMO–LUMO of UAu $_6^-$ are composed of f-orbitals, the HOMO–LUMO gaps of both majority and minority spins are quite large compared to other systems composed of d-orbitals. 30,31

3.2. Geometry and Stability of Two-Dimensional UX₄ (X = Cu, Ag, Au) Monolayers. To see if these clusters can be used as building blocks of materials where the properties of clusters will remain intact, we constructed three atomic thick hexagonal 2D structures composed of uranium and coinage metal atoms. In monolayer, UX₄, a triangular network of U atoms is sandwiched between two coinage metal honeycomb lattices as presented in Figure 3a. Each U atom is covalently bonded to 12 X atoms, as shown in Figure S3. The hexagonal 2D crystal structure has a P6/MMM (D_{6h}^1) symmetry group (space group number 191). The optimized geometrical parameters of the UX₄ monolayers (ML) are listed in Table 2. The bond lengths between U-X in 2D structures follow the

Table 2. DFT Optimized Geometrical Parameters of the UX_4 Unit Cell

| monolayers | a = b (Å) | bond length U-X (Å) (2D material) | bond length U-X (Å) (Anionic cluster) | vertical height (d) between U and X planes (Å) |
|------------|--------------|---|---------------------------------------|--|
| UCu_4 | 4.23 | 2.96 | 2.8 | 1.66 |
| UAg_4 | 4.74 | 3.15 | 3.07 | 1.56 |
| UAu_4 | 4.7 | 3.11 | 2.97 | 1.53 |

same trend as in clusters. Notably, the bond length and the lattice constants of the UAg₄ monolayer are larger compared to the UAu₄ monolayer, the difference originating from the larger atomic radius of Ag compared to that of Au. The vertical distances between the U atom and the coinage metal planes, as indicated in Figure 3a, decrease from Cu to Au in the 2D structures. This too is consistent with results from the corresponding clusters. We note that the UAu₂ crystal^{32,33} has been experimentally synthesized in which the uranium

atom is covalently bonded to 12 Au-atoms. The geometrical view is plotted in Figure S3.

Next, the dynamical stability of the designed 2D monolayers has been confirmed from the phonon dispersion plot presented in Figure 3b. Analysis of the phonon spectra shows that all 15 phonon branches (three acoustic and 12 optical) have positive frequencies. A quadratic dispersion of three acoustic branches near the Γ -point is observed which is essential in a dynamically stable structure. ^{34–36}

3.3. Magnetic Properties and Spin Exchange Interaction. The spin-polarized calculations carried out without (with) spin-orbit coupling (SOC) yield an on-site magnetic moment of $2.2\mu_{\rm B}$ ($1.62\mu_{\rm B}$), $2.72\mu_{\rm B}$ ($2.35\mu_{\rm B}$) and $2.47\mu_{\rm B}$ ($2.08\mu_{\rm B}$) in UCu₄, UAg₄, and UAu₄ 2D monolayers. The magnetic moments are localized at the U atom site in the unit cell as can be visualized in Figure 3c. The percentage orbital contribution to magnetic moment is provided in Table S5. The magnetic moment of the uranium atom in the bulk UAu₂ structure is calculated to be $2.44\mu_{\rm B}$, as indicated in Figure S3. Figure 3d represents the spin density (ρ_{\uparrow} - ρ_{\downarrow}) of the UAu₄ ML, suggesting that the magnetism originates entirely from the U atoms whereas the Au atom remains nonmagnetic.

To investigate the spin exchange coupling for 2D monolayers, both ferromagnetic (FM) and antiferromagnetic (AFM) couplings between the nearest-neighbor U atoms are considered. Assuming that the nearest neighbors $\langle ij \rangle$ have the same interaction strength, the magnetic coupling Hamiltonian³⁷ can be written as

$$H = E_0 - J \sum_{\langle ij \rangle} \sigma_i \sigma_j \tag{2}$$

where $\sigma_i \in \{-1, +1\}$ represents Ising spins, J is the exchange energy between the neighboring site indicated in Figure 3e, $\langle ij \rangle$ represents the sum over all nearest neighbors, and E_0 represents the nonmagnetic part of the energy. In the case of a positive exchange integral J > 0, the system is in a ferromagnetic ground state such as $|\uparrow\uparrow\uparrow\uparrow\rangle$ or $|\downarrow\downarrow\downarrow\downarrow\rangle$. In contrast, when the exchange integral is negative J < 0, nearestneighbor magnetic moments tend to align antiferromagneti-

cally in the form $|\uparrow\downarrow\uparrow\rangle$. 38,39 A 2 × 2 supercell is constructed from the optimized unit cell to study the preferred magnetic ground state. The magnetic configurations and projected magnetization of the spin density along the *z*-direction for FM and AFM are shown in Figure 3e, f. The total energy of 2 × 2 supercells in their FM and AFM states can be expressed as

$$E_{\rm FM} = E_0 - 3J \tag{3}$$

$$E_{AFM} = E_0 + J \tag{4}$$

The magnetic exchange coupling constants per unit cell can be calculated using the following relation:

$$J = \frac{\Delta E_{\rm ex}}{4 \times 4} \tag{5}$$

The energy differences between AFM and FM magnetic configurations are summarized in Table 3. Both spin-polarized

Table 3. Calculated Exchange Energy and Magnetic Coupling Constant Per Unit Cell

| | $\Delta E_{\rm ex} = E_{\rm AFM} - E_{\rm FM} \ ({\rm meV})$ | | J (meV/unit cell) | |
|------------|--|----------|-------------------|----------|
| monolayers | without SOC | with SOC | without SOC | with SOC |
| UCu_4 | -14.4 | -33.02 | -0.9 | -2.06 |
| UAg_4 | -202.19 | -137.4 | -12.63 | -8.58 |
| UAu_4 | -170.94 | -109.68 | -10.68 | -6.85 |

and noncollinear DFT calculations suggest that all three monolayers, UCu₄, UAg₄, and UAu₄, prefer antiferromagnetic configuration, as indicated by the negative value of the exchange energy. Among the three pristine monolayers, the magnitude of $|\Delta E_{\rm ex}|$ is the smallest for UCu₄ and the largest for UAg₄ which can be correlated to the size of Cu/Ag/Au. The exchange energy and J values are further calculated using meta-GGA and are listed in Table S6. We have also performed energy calculations considering different orientations of the magnetic moments for AFM as schematically shown in Figure 4a,b for the UAu₄ monolayer. The AFM state is always found to be lower in energy by 0.171 eV than the FM state. The energy of all the five AFM configurations is found to be the same.

3.4. Electronic Properties. The spin-polarized band structures in the AFM state are plotted in Figure 4 which indicates that the systems are metallic. The atom and orbitalprojected band structures indicate that the bands near the Fermi level are mainly composed of U: f and Au: p (see Figure 4c,d) where the U: f states are found to be more dominant. The projected band structure depicts U: f and Au: p orbitals hybridizing near/above the Fermi level which provides an extra channel for indirect coupling between two neighboring U atoms through the Au-atom. Furthermore, all Au: p orbitals $(p_x, p_y, \& p_z)$ are projected into the band structure in Figure 4e which shows a significant contribution of p_x and p_z but a slightly lower contribution of p_{ν} in the energy window of [-0.5, 0.5] eV. These conduction electrons mediate indirect spin-spin coupling between U atoms through the Au atom. Similar electronic properties are observed for UAg₄ ML (see Figure 4f-h).

3.5. Magnetic Anisotropy Energy. The magnetic anisotropy energies (MAE = $E_{\perp} - E_{\parallel}$; E_{\perp} and E_{\parallel} represent total energies for the spin direction along the z and xy plane, respectively) of monolayers are calculated to be 8.28, 2.7, and

5.49 meV/atom for UCu₄, UAg₄, and UAu₄ monolayers, respectively. The easy axis is found to be in-plane for all the monolayers. For comparison, the MAE of other 2D materials is 0.22 meV/atom for MnB and 0.48 meV/atom for FeB monolayers. The monolayers MnB and FeB have magnetic moments of $5\mu_B$ and $3\mu_B$, respectively. However, the origin of magnetism in those systems is from partially filled d-orbitals, whereas for 2D materials studied in this work, they are from partially filled f-orbitals which have higher energy.

3.6. Ground-State Magnetic Properties of Hydrogenated UX₄ (X = Ag, Au) Monolayers. Since the ground state of UX₄ monolayers is antiferromagnetic, we have examined if some strategy can make them ferromagnetic. We note that one of the earlier studies predicted that graphene can be ferromagnetic once it is semihydrogenated (called graphone). Verification of this prediction by later experiments has led to the use of hydrogen as a means to transform antiferromagnetic monolayers such as CrSe₂, and CrTe₂ to a ferromagnetic state. These results demonstrated that hydrogenation leads to an expansion of the unit cell volume and drives the system toward ferromagnetic ordering as observed experimentally.

Here, we have examined if the hydrogenation of UAg₄ and UAu₄ monolayers could also lead to an antiferromagnetic to ferromagnetic transition. We focused on these two systems as the energy difference between the AFM and FM configurations is much larger than that of the UCu₄ 2D monolayer. The geometrical view of the fully hydrogenated monolayers is presented in Figure 5a. A comparison of optimized lattice constants before and after hydrogenation is presented in Table 4. The lattice constants increase with hydrogenation, leading to an expansion of the unit cell by 2.7 and 3.14% for UAg4 and UAu₄ monolayers, respectively. DFT calculation indicates that the total energy of the system is minimum when the H atom is adsorbed by the X atom compared to the U atom. The exchange energies of these hydrogenated monolayers are calculated using a 2 × 2 supercell for the FM and AFM configurations. The results are listed in Table S7. The antiferromagnetic coupling constant J decreases as the hydrogenation percentage increases and finally the magnetic ordering transforms from the antiferromagnetic to the ferromagnetic state. The spin density and projected magnetization along the z-direction of both UAg₄H₄ and UAu₄H₄ in FM configuration are plotted in Figure 5a,b. The Curie temperature that corresponds to the transition from the ferromagnetic to the paramagnetic phase is calculated using Monte Carlo (MC) simulations. The average magnetic moment at different temperatures has been evaluated based on the classical spin-half Ising model. In the MC simulations, a 30×30 supercell is used to calculate the Curie temperature. At each temperature, 10⁵ loops are taken to achieve an average magnetic moment value.

The Curie temperatures of UAg_4H_4 and UAu_4H_4 monolayers have been calculated using MC simulation; their variation of magnetization with temperature is provided in Figure 5c. The Curie temperatures of both monolayers are calculated to be ~210 K, which is greater than the MnO₂ monolayer⁴⁵ (140 K) and comparable to the FeC₂ monolayer⁴⁶ (245 K), $Cr@gtC_3N_3$ (325 K),⁴⁷ and MnB monolayer⁴⁸ (345 K), $ScCr_2C_2^{49}$ (187 K), Cr_2O_3 (185 K).³⁹ Nearly the same value of the Curie temperature for both UAg_4H_4 and UAu_4H_4 monolayers is due to approximately the same lattice constant (see Table 4) and J value (see Table S7).

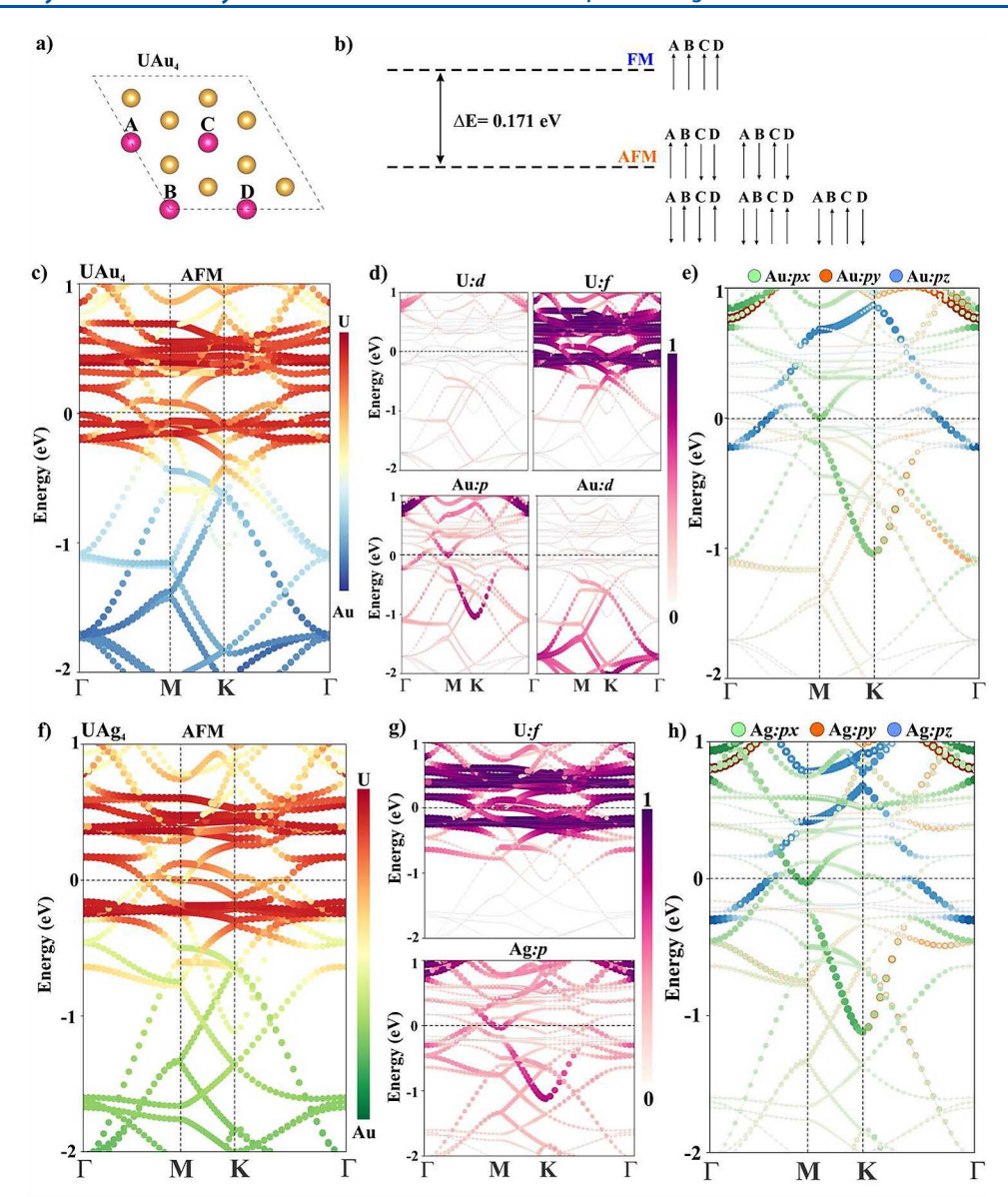


Figure 4. (a) 2×2 supercell of UAu₄ monolayer; four uranium atoms are labeled as A/B/C/D, (b) comparative energy difference for different magnetic orientations; 5 configurations are considered for the AFM state as schematically presented, (c-e) atom/orbital projected band structure of the UAu₄ supercell in the AFM configuration; Fermi level is set to zero, (f-h) atom/orbital projected band structure of the UAg₄ supercell in the AFM configuration.

To further illustrate the phase transition from the AFM to the FM state with hydrogenation, we plot the deformation charge density, as shown in Figure 5d. The deformation charge density shows the accumulation of the electrons around the adsorbed H atom while electronic charge depletion from both the UAg₄ and UAu₄ layers suggests electron transfer from the UAg₄/UAu₄ layer to the H-atoms. Therefore, the adsorbed H atom reduces the electronic charge density from the UAg₄/UAu₄ layer, mimicking the hole doping condition. The electron charge transfer per atom obtained from Bader charge analysis is listed in Table 5 and exhibits the same trend.

For a systematic comparison, the effect of hydrogenation on the electronic properties of pristine and hydrogenated monolayers is studied and the corresponding DOS with and without hydrogenation are plotted in Figure S4. The higher energy electronic states in pristine monolayers are quenched with the addition of hydrogen which is consistent with the hole doping condition. In other words, the transport properties of conduction electrons are greatly affected by hydrogenation, and the antiferromagnetic to ferromagnetic transition under these circumstances provides a qualitative picture of the existence of an indirect exchange interaction between electron spins localized at the U-sites. Magnetism induced in these metallic systems due to f-orbitals of the U atom and the spin density localized at the U atom site can be attributed to the Ruderman–Kittle–Kasuya–Yosida (RKKY)-type indirect exchange interaction ^{51,52} between neighboring electron spins through the conduction electrons.

Further DFT calculations are performed to analyze the origin of phase transition and to confirm the type of magnetic exchange interaction. As hydrogen leads to an expansion of the lattice and magnetic transition, we wondered if the antiferromagnetic to ferromagnetic transition could also be induced by applying only biaxial strain to the pristine monolayers. To address this question, we studied the variation of the magnetic coupling constant *J* for UAg₄ and UAu₄

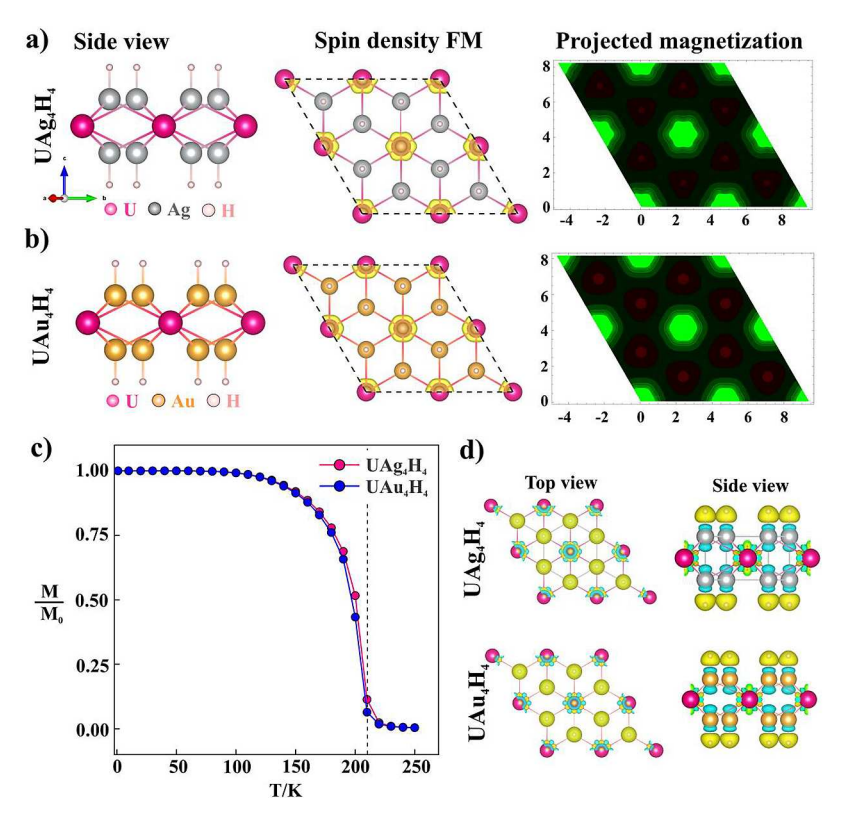


Figure 5. Geometrical side view, spin density in FM configuration and projected magnetization of spin density along the z-direction of (a) UAg_4H_4 and (b) UAu_4H_4 monolayer, (c) Variation of total magnetic moment per unit cell of fully hydrogenated UAg_4 and UAu_4 monolayers, and (d) top view of the 3D iso-surface (0.007 e/ų) of the charge density difference; yellow and cyan color represent charge accumulation and depletion, respectively.

Table 4. Comparison of the Optimized Lattice Constants of 2D Materials with Varying Degrees of Hydrogenation

| 2D system | pristine | one side- hydrogenation | both side-hydrogenation and % expansion of unit cell |
|------------------|----------|----------------------------|--|
| UAg ₄ | 4.742 | 4.867 | 4.87 (2.7%) |
| UAu_4 | 4.704 | 4.847 | 4.852 (3.14%) |

Table 5. Electronic Charge Transfer (e/atom) of U, X (Cu, Ag, Au), and H

| | $\Delta Q_{ m U}$ | ΔQ_{X} | $\Delta Q_{\rm H}$ (e/H) |
|------------|-------------------|-------------------------|--------------------------|
| UAg_4 | -1.4 | +0.35 | |
| UAg_4H_2 | -1.29 | +0.19 | +0.43 |
| UAg_4H_4 | -1.39 | -0.093 | +0.442 |
| UAu_4 | -1.957 | +0.49 | |
| UAu_4H_2 | -2.037 | +0.26 | +0.49 |
| UAu_4H_4 | -1.88 | -0.062 | +0.53 |

pristine monolayers under applied strain, $\epsilon = \frac{a-a_0}{a_0}$, where a_0 and a are the unstrained and strained lattice constants, respectively. The results are plotted in Figure S5 in the SI. Although it shows a clear variation, the J values are still negative even with a large biaxial strain of $\sim 10\%$. Furthermore, the magnetic coupling constants J calculated by removing the hydrogen atoms from hydrogenated UAg₄ and UAu₄ monolayer structure but maintaining the same expanded structure are found to be -15.65 meV/unit cell for the UAg₄ monolayer and -9.99 meV/unit cell for the UAu₄ monolayer. The negative value of J indicates that the AFM state is energetically preferred. These results confirm that the

origin of the magnetic phase transition lies in the electronic interaction between adsorbed hydrogen atom and the UX4 monolayer i.e., electronic charge transfer from UAg₄/UAu₄ to hydrogen atom plays a decisive role in these phase transitions, not just an expansion of the unit cell. Hydrogenation lowers the number of conduction electrons of UAg₄ and UAu₄ monolayers as a clear difference can be observed in the DOS plot (see Figure S4) and from the data obtained in Bader charge analysis; charge deficiency is ~1e and ~2e on the U atom (see Table 5) in UAg₄H₄ and UAu₄H₄ monolayer, respectively. These results are consistent with the previous experiment on other materials.⁵³ The surfaces of the 2D monolayers are Ag/Au atoms, which are noble metal atoms, and hence, they interact weakly with hydrogen. Nevertheless, we performed MD simulation at 300 K for 2 ps and present the results in Figure S6. The hydrogen atoms can be seen to remain near the surfaces. No significant distortion of the designed 2D structures is observed. The energy profile varies significantly in the hydrogenated UAu₄ case because of the very weak interaction of H atoms with Au compared to that of Ag. Hence, instead of hybrid functionals or meta-GGA, we have calculated the energy exchange parameters using different U_{eff} values (U_{eff} = 3 eV) and listed the results in Table S8. The $\Delta E_{\rm ex}$ and J values vary slightly.

For a better understanding of the AFM state in pristine and the FM state in hydrogenated MLs, U: f projected band structures are plotted in Figure 6a,b. For a systematic comparison, a slightly different energy window is considered. The higher energy U: f bands become localized as Au is substituted by Cu which provides a hint toward FM ordering as quantified by J values: UAu₄ (JJ = 10.68 meV) > UCu₄ (JJ =

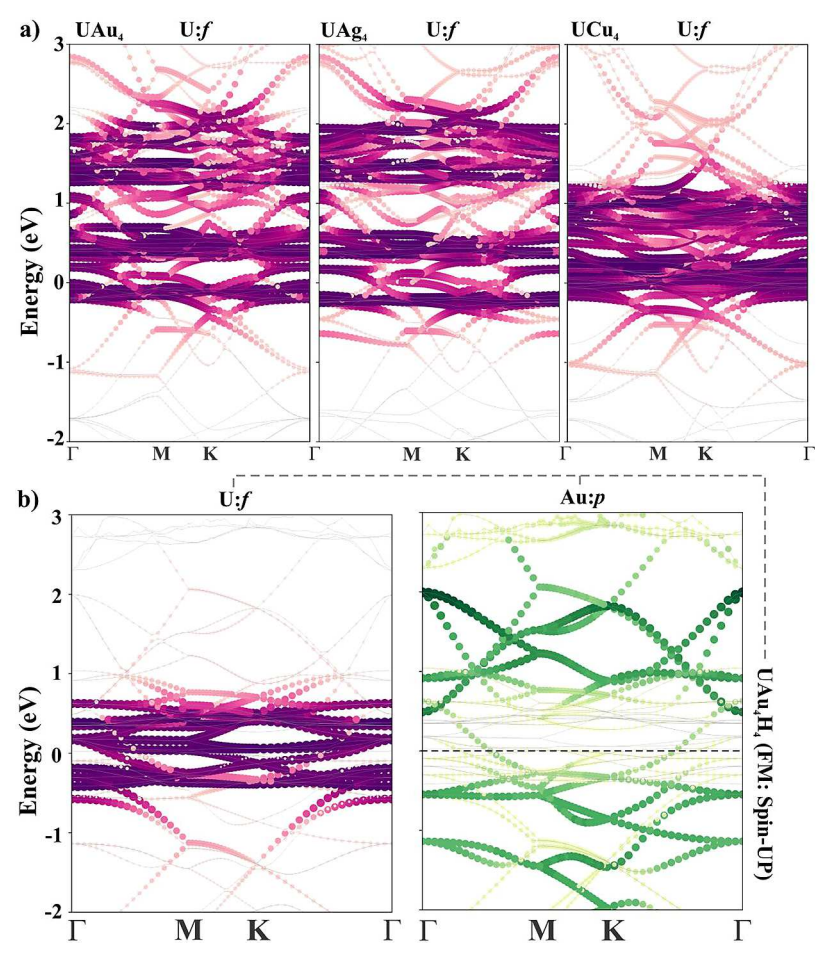


Figure 6. Orbital projected band structure of (a) pristine ML (AFM: spin-UP) and (b) hydrogenated ML (FM: spin-UP).

0.9 meV). Furthermore, Figure 6b shows that when UAu₄ ML is hydrogenated, U: f becomes more localized due to charge deficiency as mentioned earlier, and sandwiched between lower and higher energy Au: p bands. This will provide more channels for indirect coupling between the uranium atoms. The localization of U: f bands near the Fermi level gives a clear picture of the AFM to the FM transitions upon hydrogenation. In other words, in pristine U: f, bands hybridize with only higher energy Au: p bands whereas in hydrogenated MLs, U: f bands can interact with both higher and lower energy Au: p bands which leads to the AFM to the FM transition.

4. CONCLUSIONS

In summary, inspired by the recent experimental work on magnetic UAu₆ cluster, calculations on a series of iso-structural and iso-electronic clusters composed of one uranium atom and six coinage metal atoms (UX₆: X = Cu, Ag) have been carried out. The DFT calculations indicate that anionic UCu₆⁻ and UAg₆⁻ clusters have quartet spin multiplicity similar to that observed in the UAu₆⁻ cluster. A magnetic moment of $3\mu_B$ is found in these clusters, originating from the unoccupied forbitals of the uranium atom.

To see if the structure and magnetism of these clusters can be retained in a periodic crystal structure, we have designed a series of three atomic-thick UX_4 (X = Cu, Ag, Au) monolayers. These structures are found to be thermodynamically and dynamically stable where the underlying cluster geometry as well as its magnetism is retained. However, two atomic-thick

UX₂ monolayers are found to be dynamically unstable. The ground state of all three monolayers is found to be antiferromagnetic as confirmed by spin-polarized calculations including spin-orbit coupling (SOC) and meta-GGA (SCAN). Although the interaction between hydrogen atoms and Ag/Au surfaces is weak, antiferromagnetic to ferromagnetic phase transition can be achieved via hydrogenation. The Curie temperatures of fully hydrogenated UAg₄ and UAu₄ monolayers are calculated using Monte Carlo simulation and found to be ~210 K for both cases. From the optimized lattice constants of 2D monolayers with and without hydrogenation, we observe that hydrogenation leads to unit cell expansion, lowers the conduction electron density from the uranium atom, and drives the system toward ferromagnetic ordering. The long-range RKKY-type exchange interaction between neighboring spins is found to be dominant in these metallic systems. This is consistent with experimental observation in other systems. Most importantly, these results, inspired by the lessons from cluster science, show that new materials can be formed with clusters as building blocks. A recent experimental observation³² of nonfermi liquid behavior of bulk UAu₂ structures below Ne'el temperature provides a new platform to study the same in these strongly correlated 2D electron systems.

ASSOCIATED CONTENT

Supporting Information

The Supporting Information is available free of charge at https://pubs.acs.org/doi/10.1021/acs.jpcc.4c03592.

Electronic structure analysis of UCu₆⁻ and UAg₆⁻, geometrical view of U-Au bonds, variation of magnetic coupling constant (J) of pristine UAg₄ and UAu₄ monolayer under biaxial strain, DOS and projected DOS of pristine and hydrogenated UAg₄ and UAu₄ monolayers, AIMD simulation of (a) UAg₄, (b) UAu₄ monolayers with both sides hydrogenated, total energy of neutral and anionic clusters in Hartree unit having different spin states, NPA charge distribution and SCPA spin population of UX₆, orbital composition analysis of HOMO and LUMO with Ros-Schuit (SCPA) partition, atomic composition analysis of HOMO and LUMO, percentage orbital contribution to the magnetic moment, calculated exchange energy and magnetic coupling constant per unit cell with meta-GGA (SCAN), calculated exchange energy, magnetic coupling constant per unit cell, and Curie temperature obtained from the Monte Carlo simulation, and calculated exchange energy and magnetic coupling constant per unit cell with GGA-PBE with $U_{\text{eff}} = 3 \text{ eV (PDF)}$

AUTHOR INFORMATION

Corresponding Author

Puru Jena — Department of Physics, Virginia Commonwealth University, Richmond, Virginia 23284, United States; orcid.org/0000-0002-2316-859X; Email: pjena@vcu.edu

Author

Manish Kumar Mohanta — Department of Physics, Virginia Commonwealth University, Richmond, Virginia 23284, United States; orcid.org/0000-0002-5476-8336

Complete contact information is available at: https://pubs.acs.org/10.1021/acs.jpcc.4c03592

Notes

The authors declare no competing financial interest.

ACKNOWLEDGMENTS

The work was partially supported by the U.S. Department of Energy, Office of Basic Energy Sciences, Division of Materials Sciences and Engineering under Award No. DE-FG02-96ER45579. Resources of the National Energy Research Scientific Computing (NERSC) Center supported by the Office of Science of the U.S. Department of Energy under Contract No. DE-AC02-05CH11231 is also acknowledged. The authors extend their acknowledgment to the High-Performance Research Computing (HPRC) core facility at Virginia Commonwealth University for providing supercomputing resources.

REFERENCES

- (1) Rao, B. K.; Jena, P.; Manninen, M. Relationship between Topological and Magnetic Order in Small Metal Clusters. *Phys. Rev. B* **1985**, 32 (1), 477–479.
- (2) Sun, H.; Luo, Y.-H.; Zhao, J.; Wang, G. Structural, Electronic, and Magnetic Properties of Small Vanadium Clusters. *Phys. Status Solidi B* **1999**, 215 (2), 1127–1135.

- (3) Zhao, J.; Chen, X.; Sun, Q.; Liu, F.; Wang, G.; Lain, K. D. Tight-Binding Study of the Structural and Magnetic Properties of Vanadium Clusters. *Phys. B Condens. Matter* **1995**, *215* (4), 377–382.
- (4) Liu, F.; Khanna, S. N.; Jena, P. Magnetism in Small Vanadium Clusters. *Phys. Rev. B* **1991**, *43* (10), 8179–8182.
- (5) Kandalam, A. K.; Rao, B. K.; Jena, P.; Pandey, R. Geometry and Electronic Structure of Vn(Bz)m Complexes. *J. Chem. Phys.* **2004**, *120* (22), 10414–10422.
- (6) Cox, A. J.; Louderback, J. G.; Apsel, S. E.; Bloomfield, L. A. Magnetism in 4d-Transition Metal Clusters. *Phys. Rev. B* **1994**, 49 (17), 12295–12298.
- (7) Cox, A. J.; Louderback, J. G.; Bloomfield, L. A. Experimental Observation of Magnetism in Rhodium Clusters. *Phys. Rev. Lett.* **1993**, 71 (6), 923–926.
- (8) Reddy, B. V.; Khanna, S. N.; Dunlap, B. I. Giant Magnetic Moments in 4d Clusters. *Phys. Rev. Lett.* **1993**, *70* (21), 3323–3326.
- (9) Apsel, S. E.; Emmert, J. W.; Deng, J.; Bloomfield, L. A. Surface-Enhanced Magnetism in Nickel Clusters. *Phys. Rev. Lett.* **1996**, 76 (9), 1441–1444.
- (10) Billas, I. M. L.; Châtelain, A.; de Heer, W. A. Magnetism from the Atom to the Bulk in Iron, Cobalt, and Nickel Clusters. *Science* **1994**, 265 (5179), 1682–1684.
- (11) Harris, R. M.; Zhu, Z.; Deepika; Tufekci, B. A.; Peterson, K.; Jena, P.; Bowen, K. H. Au as a Surrogate for F: The Case of UAu6 vs UF6. J. Am. Chem. Soc. 2022, 144 (43), 19685–19688.
- (12) Frisch, M. J.; Trucks, G. W.; Schlegel, H. B.; Scuseria, G. E.; Robb, M. A.; Cheeseman, J. R.; Scalmani, G.; Barone, V.; Petersson, G. A.; Nakatsuji, H.; Li, X.; Caricato, M.; Marenich, A. V; Bloino, J.; Janesko, B. G.; Gomperts, R.; Mennucci, B.; Hratchian, H. P.; Ortiz, J. V; Izmaylov, A. F.; Sonnenberg, J. L.; Williams-Young, D.; Ding, F.; Lipparini, F.; Egidi, F.; Goings, J.; Peng, B.; Petrone, A.; Henderson, T.; Ranasinghe, D.; Zakrzewski, V. G.; Gao, J.; Rega, N.; Zheng, G.; Liang, W.; Hada, M.; Ehara, M.; Toyota, K.; Fukuda, R.; Hasegawa, J.; Ishida, M.; Nakajima, T.; Honda, Y.; Kitao, O.; Nakai, H.; Vreven, T.; Throssell, K.; Montgomery, Jr., J. A.; Peralta, J. E.; Ogliaro, F.; Bearpark, M.; S-19, J.; Heyd, J. J.; Brothers, E. N.; Kudin, K. N.; Staroverov, V. N.; Keith, T. A.; Kobayashi, R.; Normand, J.; Raghavachari, K.; Rendell, A. P.; Burant, J. C.; Iyengar, S. S.; Tomasi, J.; Cossi, M.; Millam, J. M.; Klene, M.; Adamo, C.; Cammi, R.; Ochterski, J. W.; Martin, R. L.; Morokuma, K.; Farkas, O.; Foresman, J. B.; Fox, D. J. Gaussian 16 Revision A.03; Gaussian, Inc.: Wallingford, CT, 2016.
- (13) Becke, A. D. Density-functional Thermochemistry. II. The Effect of the Perdew-Wang Generalized-gradient Correlation Correction. *J. Chem. Phys.* **1992**, *97* (12), 9173–9177.
- (14) Becke, A. D. Density-functional Thermochemistry. III. The Role of Exact Exchange. *J. Chem. Phys.* **1993**, *98* (7), 5648–5652.
- (15) Peterson, K. A.; Puzzarini, C. Systematically Convergent Basis Sets for Transition Metals. II. Pseudopotential-Based Correlation Consistent Basis Sets for the Group 11 (Cu, Ag, Au) and 12 (Zn, Cd, Hg) Elements. *Theor. Chem. Acc.* **2005**, *114*, 283–296.
- (16) Peterson, K. A. Correlation Consistent Basis Sets for Actinides. I. The Th and U Atoms. *J. Chem. Phys.* **2015**, 142 (7), No. 074105.
- (17) Dolg, M.; Cao, X. Accurate Relativistic Small-Core Pseudopotentials for Actinides. Energy Adjustment for Uranium and First Applications to Uranium Hydride. *J. Phys. Chem. A* **2009**, 113 (45), 12573–12581.
- (18) Figgen, D.; Rauhut, G.; Dolg, M.; Stoll, H. Energy-Consistent Pseudopotentials for Group 11 and 12 Atoms: Adjustment to Multi-Configuration Dirac—Hartree—Fock Data. *Chem. Phys.* **2005**, 311 (1), 227–244.
- (19) Lu, T.; Chen, F. Multiwfn: A Multifunctional Wavefunction Analyzer. J. Comput. Chem. 2012, 33 (5), 580-592.
- (20) Kresse, G.; Furthmüller, J. Efficient Iterative Schemes for Ab Initio Total-Energy Calculations Using a Plane-Wave Basis Set. *Phys. Rev. B* **1996**, 54 (16), 11169–11186.
- (21) Kresse, G.; Furthmüller, J. Efficiency of Ab-Initio Total Energy Calculations for Metals and Semiconductors Using a Plane-Wave Basis Set. *Comput. Mater. Sci.* **1996**, *6* (1), 15–50.

- (22) Blöchl, P. E. Projector Augmented-Wave Method. *Phys. Rev. B* **1994**, *50* (24), 17953–17979.
- (23) Perdew, J. P.; Burke, K.; Ernzerhof, M. Generalized Gradient Approximation Made Simple. *Phys. Rev. Lett.* **1996**, 77 (18), 3865–3868.
- (24) Dudarev, S. L.; Botton, G. A.; Savrasov, S. Y.; Humphreys, C. J.; Sutton, A. P. Electron-Energy-Loss Spectra and the Structural Stability of Nickel Oxide: An LSDA+U Study. *Phys. Rev. B* **1998**, *57* (3), 1505–1509.
- (25) Togo, A.; Tanaka, I. First Principles Phonon Calculations in Materials Science. *Scr. Mater.* **2015**, *108*, 1–5.
- (26) Wang, V.; Xu, N.; Liu, J.-C.; Tang, G.; Geng, W.-T. VASPKIT: A User-Friendly Interface Facilitating High-Throughput Computing and Analysis Using VASP Code. *Comput. Phys. Commun.* **2021**, 267, No. 108033
- (27) Humphrey, W.; Dalke, A.; Schulten, K. VMD: Visual Molecular Dynamics. *J. Mol. Graph.* **1996**, *14* (1), 33–38.
- (28) Hanwell, M. D.; Curtis, D. E.; Lonie, D. C.; Vandermeersch, T.; Zurek, E.; Hutchison, G. R. Avogadro: An Advanced Semantic Chemical Editor, Visualization, and Analysis Platform. *J. Cheminformatics* **2012**, *4* (1), 17.
- (29) Momma, K.; Izumi, F. It VESTA3 for Three-Dimensional Visualization of Crystal, Volumetric and Morphology Data. *J. Appl. Crystallogr.* **2011**, *44* (6), 1272–1276.
- (30) Cui, C.; Zhang, H.; Gu, Y.; Geng, L.; Jia, Y.; Lin, S.; Ma, J.; Luo, Z. Tailoring Titanium Carbide Clusters for New Materials: From Met-Cars to Carbon-Doped Superatoms. *J. Am. Chem. Soc.* **2024**, *146* (13), 9302–9310.
- (31) Geng, L.; Sengupta, T.; Li, X.; Cui, C.; Lin, S.; Xu, X.-L.; Reber, A. C.; Khanna, S. N.; Zheng, W.-J.; Luo, Z. Unusually High-Spin Fe12C12— Metallo-Carbohedrene Clusters. *J. Am. Chem. Soc.* **2023**, 145 (49), 26908–26914.
- (32) O'Neill, C. D.; Schmehr, J. L.; Keen, H. D. J.; Pritchard Cairns, L.; Sokolov, D. A.; Hermann, A.; Wermeille, D.; Manuel, P.; Krüger, F.; Huxley, A. D. Non-Fermi Liquid Behavior below the Néel Temperature in the Frustrated Heavy Fermion Magnet UAu2. *Proc. Natl. Acad. Sci. U. S. A.* **2021**, *118* (49), No. e2102687118.
- (33) Pöttgen, R.; Tran, V. H.; Hoffmann, R.-D.; Kaczorowski, D.; Troc, R. Crystal Structure and Physical Properties of UAuSi and UAu2. *J. Mater. Chem.* **1996**, *6* (3), 429–434.
- (34) Mohanta, M. K.; Sarkar, A. D. Tweaking the Physics of Interfaces between Monolayers of Buckled Cadmium Sulfide for a Superhigh Piezoelectricity, Excitonic Solar Cell Efficiency, and Thermoelectricity. ACS Appl. Mater. Interfaces 2020, 12 (15), 18123–18137.
- (35) Mohanta, M. K.; IS, F.; De Sarkar, A. Valley Hall Effect in Graphene-like SnX (X = Si, Ge) Buckled Monolayers with High Charge Carrier Mobility and Low Lattice Thermal Conductivity. *Phys. Rev. B* **2023**, *107* (3), No. 035429.
- (36) Mohanta, M. K.; Arora, A.; De Sarkar, A. Effective Modulation of Ohmic Contact and Carrier Concentration in a Graphene-MgX (X = S, Se) van Der Waals Heterojunction with Tunable Band-Gap Opening via Strain and Electric Field. *Phys. Rev. B* **2021**, *104* (16), No. 165421.
- (37) Siriwardane, E. M. D.; Karki, P.; Loh, Y. L.; Çakır, D. Strain—Spintronics: Modulating Electronic and Magnetic Properties of Hf2MnC2O2MXene by Uniaxial Strain. *J. Phys. Chem. C* **2019**, *123* (19), 12451–12459.
- (38) Baltz, V.; Manchon, A.; Tsoi, M.; Moriyama, T.; Ono, T.; Tserkovnyak, Y. Antiferromagnetic Spintronics. *Rev. Mod. Phys.* **2018**, 90 (1), No. 015005.
- (39) Hashmi, A.; Nakanishi, K.; Farooq, M. U.; Ono, T. Ising Ferromagnetism and Robust Half-Metallicity in Two-Dimensional Honeycomb-Kagome Cr2O3 Layer. *Npj 2D Mater. Appl.* **2020**, *4* (1), 39
- (40) Wang, S.; Miao, N.; Su, K.; Blatov, V. A.; Wang, J. Discovery of Intrinsic Two-Dimensional Antiferromagnets from Transition-Metal Borides. *Nanoscale* **2021**, *13* (17), 8254–8263.

- (41) Zhou, J.; Wang, Q.; Sun, Q.; Chen, X. S.; Kawazoe, Y.; Jena, P. Ferromagnetism in Semihydrogenated Graphene Sheet. *Nano Lett.* **2009**, *9* (11), 3867–3870.
- (42) González-Herrero, H.; Gómez-Rodríguez, J. M.; Mallet, P.; Moaied, M.; Palacios, J. J.; Salgado, C.; Ugeda, M. M.; Veuillen, J.-Y.; Yndurain, F.; Brihuega, I. Atomic-Scale Control of Graphene Magnetism by Using Hydrogen Atoms. *Science* **2016**, 352 (6284), 437–441.
- (43) Alsubaie, M.; Tang, C.; Wijethunge, D.; Qi, D.; Du, A. First-Principles Study of the Enhanced Magnetic Anisotropy and Transition Temperature in a CrSe2Monolayer via Hydrogenation. *ACS Appl. Electron. Mater.* **2022**, *4* (7), 3240–3245.
- (44) Chevalier, B.; Pasturel, M.; Bobet, J.-L.; Etourneau, J. Antiferromagnetic–Ferromagnetic Transition Induced by the Hydrogenation of the Ternary Stannide Ce(Ni0.82Cu0.18)Sn. *Solid State Commun.* **2004**, 129 (3), 179–182.
- (45) Kan, M.; Zhou, J.; Sun, Q.; Kawazoe, Y.; Jena, P. The Intrinsic Ferromagnetism in a MnO2Monolayer. *J. Phys. Chem. Lett.* **2013**, 4 (20), 3382–3386.
- (46) Zhao, T.; Zhou, J.; Wang, Q.; Kawazoe, Y.; Jena, P. Ferromagnetic and Half-Metallic FeC2Monolayer Containing C2 Dimers. ACS Appl. Mater. Interfaces 2016, 8 (39), 26207–26212.
- (47) Choudhuri, I.; Garg, P.; Pathak, B. TM@gt-C3N3Monolayers: High-Temperature Ferromagnetism and High Anisotropy. *J. Mater. Chem. C* **2016**, *4* (35), 8253–8262.
- (48) Jiang, Z.; Wang, P.; Jiang, X.; Zhao, J. MBene (MnB): A New Type of 2D Metallic Ferromagnet with High Curie Temperature. *Nanoscale Horiz* **2018**, 3 (3), 335–341.
- (49) Zhang, Y.; Cui, Z.; Sa, B.; Miao, N.; Zhou, J.; Sun, Z. Computational Design of Double Transition Metal MXenes with Intrinsic Magnetic Properties. *Nanoscale Horiz* **2022**, *7* (3), 276–287.
- (50) Zhang, L.; Tang, C.; Sanvito, S.; Gu, Y.; Du, A. Hydrogen-Intercalated 2D Magnetic Bilayer: Controlled Magnetic Phase Transition and Half-Metallicity via Ferroelectric Switching. ACS Appl. Mater. Interfaces 2022, 14 (1), 1800–1806.
- (51) Ruderman, M. A.; Kittel, C. Indirect Exchange Coupling of Nuclear Magnetic Moments by Conduction Electrons. *Phys. Rev.* **1954**, *96* (1), 99–102.
- (52) Parkin, S. S. P.; Mauri, D. Spin Engineering: Direct Determination of the Ruderman-Kittel-Kasuya-Yosida Far-Field Range Function in Ruthenium. *Phys. Rev. B* **1991**, *44* (13), 7131–7134.
- (53) Chevalier, B.; Tencé, S.; André, G.; Matar, S. F.; Gaudin, E. From Antiferromagnetic to Ferromagnetic Ordering Induced by Hydrogenation of the Compounds NdCoSi and NdCoGe. *J. Phys. Conf. Ser.* **2010**, 200 (3), No. 032012.